



Cite as

Nano-Micro Lett.

(2020) 12:128

Received: 11 March 2020

Accepted: 18 May 2020

© The Author(s) 2020

MXene-Derived Defect-Rich TiO₂@rGO as High-Rate Anodes for Full Na Ion Batteries and Capacitors

Yongzheng Fang¹, Yingying Zhang¹, Chenxu Miao¹, Kai Zhu¹ ✉, Yong Chen², Fei Du³, Jinling Yin¹, Ke Ye¹, Kui Cheng¹, Jun Yan¹, Guiling Wang¹, Dianxue Cao¹ ✉

✉ Kai Zhu, kzhu@hrbeu.edu.cn; Dianxue Cao, caodianxue@hrbeu.edu.cn

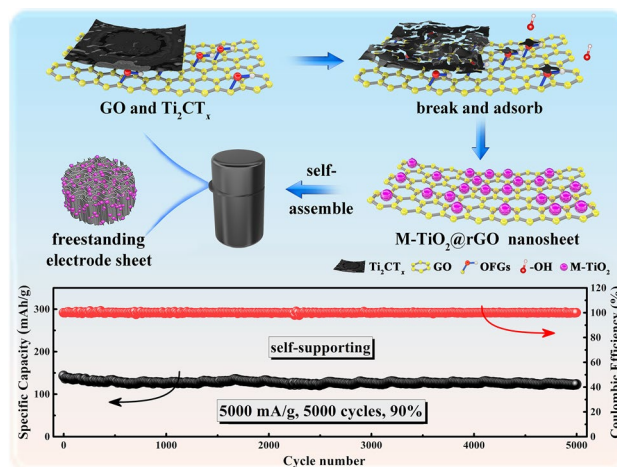
¹ Key Laboratory of Superlight Materials and Surface Technology (Ministry of Education), College of Material Science and Chemical Engineering, Harbin Engineering University, Harbin 150001, People's Republic of China² State Key Laboratory of Marine Resource Utilization in South China Sea, Hainan Provincial Key Laboratory of Research on Utilization of Si-Zr-Ti Resources, College of Materials Science and Engineering, Hainan University, 58 Renmin Road, Haikou 570228, People's Republic of China³ Key Laboratory of Physics and Technology for Advanced Batteries (Ministry of Education), College of Physics, Jilin University, Changchun 130012, People's Republic of China

HIGHLIGHTS

- A freestanding MXene-derived defect-rich TiO₂@reduced graphene oxides (M-TiO₂@rGO) foam electrode was fabricated.
- M-TiO₂@rGO presents fast Na⁺ storage kinetics due to capacitive contribution.
- M-TiO₂@rGO foam electrode displays a capacity retention of 90.7% after 5000 cycles.

ABSTRACT Sodium ion batteries and capacitors have demonstrated their potential applications for next-generation low-cost energy storage devices. These devices's rate ability is determined by the fast sodium ion storage behavior in electrode materials. Herein, a defective TiO₂@reduced graphene oxide (M-TiO₂@rGO) self-supporting foam electrode is constructed via a facile MXene decomposition and graphene oxide self-assembling process. The employment of the MXene parent phase exhibits distinctive advantages, enabling defect engineering, nanoengineering, and fluorine-doped metal oxides. As a result, the M-TiO₂@rGO electrode shows a pseudocapacitance-dominated hybrid sodium storage mechanism. The pseudocapacitance-dominated process leads to high capacity, remarkable rate ability, and superior cycling performance. Significantly, an M-TiO₂@rGO//Na₃V₂(PO₄)₃ sodium full cell and an M-TiO₂@rGO//HPAC sodium ion capacitor are fabricated to demonstrate the promising application of M-TiO₂@rGO. The sodium ion battery presents a capacity of 177.1 mAh g⁻¹ at 500 mA g⁻¹ and capacity retention of 74% after 200 cycles. The sodium ion capacitor delivers a maximum energy density of 101.2 Wh kg⁻¹ and a maximum power density of 10,103.7 W kg⁻¹. At 1.0 A g⁻¹, it displays an energy retention of 84.7% after 10,000 cycles.

KEYWORDS MXene-Ti₂CT_x; Vacancy oxygen; Self-supporting; TiO₂ anodes; Sodium ion battery and capacitor



1 Introduction

With the high-speed development of electric vehicles and smart grids, the market for electrochemical energy storage devices (EESDs) is bound to expand rapidly [1]. Due to the shortage of lithium resources, lithium-ion batteries are facing the difficulties of increasing cost and future availability [2]. Therefore, sodium ion batteries (SIBs) have attracted great interest due to their low cost and high sodium abundance [3, 4]. To date, $\text{Na}_3\text{V}_2(\text{PO}_4)_3$ with sodium super ionic conductor (NASICON) structure has been regarded as one of the most promising cathodes [5, 6]. Although NASICON-type cathodes promise fast sodium ion diffusion and high-power density, the rate performance of sodium ion full cells is hindered by the anode materials. Recently, a hybrid device called sodium ion capacitor (SIC) [7, 8] has offered another choice for EESDs, owing to its comprehensive advantages of high energy and power densities. Usually, a SIC consists of a battery-type anode and a capacitor-type cathode to bridge the strengths of SIBs and supercapacitors [9]. The key to constructing a high-performance SIC is to couple a suitable anode with a cathode, wherein they need well match in rate abilities. Thus, anode materials with fast sodium storage kinetics have become a key limitation in developing superior rate performance SIBs and SICs compared to fast energy storage cathodes.

According to the working principles, anode materials can be divided into intercalation, alloying, and conversion types [10, 11]. Usually, intercalation-type anodes avoid damaging volume expansion and contraction, which is a perplexing problem in alloying and conversion-type anodes [12]. Thus, various intercalation-type anodes have been explored for SIBs, such as hard carbon [13], layered titanium-based oxides [14], and molybdenum-based material [10]. Among these, TiO_2 is considered to be one of the most promising SIB anode materials due to its safety and low work potential relative to the Na^+/Na redox couple [15, 16]. However, its electrochemical performance is severely restricted by poor electron mobility ($\sim 10^{-12} \text{ S cm}^{-1}$) and low sodium ion diffusivity [9, 17]. Defect engineering plays an important role in improving the physical and chemical properties of metal oxides. Oxygen vacancies have recently been shown to be able to significantly enhance the electronic and ionic conductivity of TiO_2 , thus enhancing the ions storage capacity and catalytic performance [18–20]. Theoretical calculations

also indicate that oxygen vacancies can increase the number of reactive sites, decrease the reaction barrier, and improve the ionic diffusion path [19, 21]. Thus, it is an effective approach to improve the properties of TiO_2 . Another strategy, preparing nanomaterials has presented a unique advantage in shortening the sodium ion transport pathway [9, 22]. Ti-based MXene materials have been reported as a capable precursor for producing nano-Ti-based oxides and related composites owing to its two-dimensional (2D) nanosheet morphology [15, 23, 24]. However, the details of the transformation from Ti-based MXene to Ti-based oxide and the cause of MXene's instability in the water have been unclear. 2D materials were often employed to carry nanomaterials due to the large specific surface and fast ions/electrons diffusion [25–27]. Moreover, modification with carbon-based materials has been shown to be an effective solution for enhancing electron transport to achieve a high rate anode material [28, 29]. Recently, introducing a capacitive contribution has demonstrated another effective approach for overcoming poor sodium ion diffusion [7, 15, 23]. Designing defective nanomaterials can extremely enhance the capacitive contribution, leading to impressive rate performance and cycling stability [30, 31].

The architectural design of electrodes plays an important role in the performance and processing cost of batteries. Usually, the electrode is fabricated by a tedious slurry-casting process [32]. In a toxic and costly *N*-methyl pyrrolidone (NMP), the mixture of electrode materials including a conductive additive ($\sim 10 \text{ wt}\%$) and an insulating binder ($\sim 10 \text{ wt}\%$) is cast onto a heavy metal current collector. Inactive components occupy 70–80 wt% of the whole electrode, which significantly reduces the energy density and increases the cost [8, 33]. Thus, freestanding and binder-free construction could eliminate the additional inactive materials to realize a high-efficiency electrode.

Herein, a freestanding, binder-free, and defective Ti_2CT_x -MXene-derived TiO_2 complex reduced graphene oxides (M- TiO_2 @rGO) 3D foam electrode was designed and synthesized via a simple and nontoxic hydrothermal process. Ti_2CT_x -MXene was converted to M- TiO_2 by consuming the $-\text{OH}$ in the H_2O and the F functional group self-doped into the M- TiO_2 , during that a large number of lattice defects and oxygen vacancies were generated in situ. The addition of graphene oxide promoted the above reaction and constructed a 3D M- TiO_2 @graphene composite with a highly conductive pathway

and accelerated ion diffusion. Directly employed as the anode for a sodium ion half-cell, the prepared materials displayed a remarkable rate ability and stable cycling performance due to its large capacitive contribution. Significantly, this composite was a capable and universal anode for both sodium ion full cells and sodium ion capacitors with favorable cycling stability.

2 Experimental Section

2.1 Preparation of Ti_2CT_x MXene Powder

Ti_2CT_x MXene was obtained by a synthetic HF solution. Specifically, 3 g of LiF (Alfa Aesar, 98.5%) was dissolved in 30 mL HCl (12 M). Then 2 g of Ti_2AlCl (200 mesh, purchased from Forsman Scientific (Beijing) Co., Ltd.) powder was slowly added into the above mixture solution and kept at 40 °C for 36 h under stirring. After that, the solution was centrifuged several times until the PH of the supernatant was about 5–6. Particularly, the supernatant of the first centrifuge was khaki. Finally, Ti_2CT_x cake resembling graphene oxide was obtained by freeze-dried.

2.2 Preparation of M-TiO₂@rGO Foam, M-TiO₂, Na₃V₂(PO₄)₃, and HPAC

M-TiO₂@rGO foam was prepared through a simple hydrothermal reaction [15]. In the typical preparation, 120 mg Ti_2CT_x was dissolved in 40 mL distilled water and ultrasound for 3 h, then 130 mg GO (prepared from a modified Hummers method [34]) was added in it and continued ultrasound for 2 h. After that, 4 mL NaHSO₃ (0.5 mM) solution was added to the above solution as a reducing agent. Finally, the above solution was transferred to a polytetrafluoroethylene reactor and kept at 180 °C for 16 h. The obtained M-TiO₂@rGO cylindrical gel was dialyzed for 6 h in a mixture of water and ethanol. Finally, the M-TiO₂@rGO foam was obtained through a freeze-drying process.

M-TiO₂ nanoparticles were prepared under the same conditions without the addition of GO.

Na₃V₂(PO₄)₃ cathode material was prepared by the previous report [5].

3D hierarchical porous activated carbon (HPAC) derived from coir was prepared by the previous report [35].

2.3 Material Characterizations

The compositions of M-TiO₂@rGO and M-TiO₂ were characterized by X-ray diffractometer (XRD) with copper K α radiation ($\lambda = 1.5418 \text{ \AA}$) and Raman spectroscopy (RENISHAW, REF 2000, 514.5 nm laser). The surface functional groups of M-TiO₂@rGO were checked by XPS (Axis Ultra DLD, Kratos Analytical). The morphologies of the M-TiO₂@rGO, M-TiO₂, and Ti_2CT_x were analyzed by a field-emission scanning electron microscope (SEM, JEOL, JSM7500F) and a transmission electron microscope (TEM, JEOL, JEM-2100 model). Nitrogen adsorption–desorption isotherms were tested on a Quantachrome NOVA 2000e sorption analyzer at 77 K with liquid nitrogen. The rGO content of samples was tested by thermogravimetry (TA-Instruments-Wutersllc, TGA 500). The oxygen vacancies were checked through the electron paramagnetic resonance (EPR) spectra, which were recorded on a Bruker EPR ELEXSYS 500 spectrometer.

2.4 Fabrication and Electrochemical Measurements of Half Cells

The self-supporting M-TiO₂@rGO electrode sheets were obtained after freeze-drying the sheets cut from M-TiO₂@rGO gel (when it was wet). The coated M-TiO₂@rGO, HPAC, or NVP working electrodes consisted of active materials, supper P, and polyvinylidene fluoride (PVDF) (80:10:10 wt%), which were dispersed in *N*-methyl-2-pyrrolidone (NMP) uniformly. The M-TiO₂ electrode was 70:20:10 wt% to balance its carbon-free nature. The slurry was coated on the current collectors (Cu foils for M-TiO₂, M-TiO₂@rGO anodes, and Al foils for HPAC, NVP cathodes) and dried at 80 °C in vacuum for 24 h. And then, these coated electrodes were cut into a circular shape with diameters of 12 mm. The mass loading was 0.5–1 mg cm⁻² for anodes and 1–2 mg cm⁻² for cathodes. In an Ar-filled glove box, CR2023-type coin cells were assembled with the as-prepared electrodes as working electrodes, the metallic sodium as the counter electrode and reference electrode, the glass fibers (Whatman) as separators, and the 1.0 M NaClO₄ in EC: DMC: EMC = 1:1:1 vol% with 5.0% FEC as the electrolyte. The constant current charge/discharge tests were measured

at the NEWARE battery test system (CT-4008 model), and the cyclic voltammetry (CV) tests were performed at Bio-Logic VMP3 electrochemical workstation. All electrochemical measurements were tested at room temperature. The specific capacities and current densities of self-supporting M-TiO₂@rGO electrodes were calculated based on the M-TiO₂ mass (70 wt%), correspondingly, the coated M-TiO₂@rGO electrodes were calculated based on the rGO and M-TiO₂ mass (80 wt% in the total coating materials). Those in cathode electrodes (HPAC and NVP) were based on the active materials (80 wt% in the total coating materials). The voltage ranges of the M-TiO₂, M-TiO₂@rGO, HPAC, and NVP were 0.1–3.0, 0.1–3.0, 3.0–4.2, and 2.0–4.3 V, respectively.

2.5 Fabrication and Electrochemical Measurements of Full Cells of SICs and SIBs

Before assembling the full batteries, the coated M-TiO₂@rGO was activated for 5 cycles at 50 mA g⁻¹ in half cells. In the SICs, HPAC as a cathode and the coated M-TiO₂@rGO as an anode, the mass ratios were 1:1.0, 1:1.5, 1:2.0, 1:3.0 (anode: cathode), and the voltage range was 1.0–4.0 V. In the SIBs, NVP as the cathode and the coated M-TiO₂@rGO as the anode, the mass ratio was optimized at 1:3 (anode: cathode), and the voltage range was 1.0–3.5 V. The separator, electrolyte, and assembly method were the same as those in half cells.

The specific capacities of the SIBs were calculated based on the mass of the coated M-TiO₂@rGO.

The energy densities (E , Wh kg⁻¹) and power densities (P , W kg⁻¹) of the SICs were calculated by Eqs. (1) and (2):

$$E = \frac{\int_{t_1}^{t_2} IV dt}{(M_1 + M_2) * 3.6} \quad (1)$$

$$P = \frac{E}{T} \quad (2)$$

In the formulas, t_1 and t_2 are the start and end time (s) of the discharge, respectively, I (A) is the current, V (V) is the voltage at a particular time, M_1 and M_2 are the mass of anode and cathode (g), respectively, and T (h) is the total time of the discharge.

3 Results and Discussion

3.1 Synthesis and Characterization of Defective MXene-Derived TiO₂@Graphene Electrode

Ti₂CT_x-MXene-derived TiO₂ complex graphene (M-TiO₂@rGO) foam was prepared by a simple hydrothermal reaction associated with a series of transformations of Ti₂CT_x. First, Ti₂CT_x nanosheets were mixed uniformly with graphene oxide (GO) nanosheets in an ultrasonic process (Fig. 1a). Then, in a hydrothermal process, the Ti₂CT_x nanosheets broken into small lamellae and attached to the surface of GO by the inducing effect of the oxygen-containing function groups (OFGs) of the GO (Fig. 1b). As the reaction continued, the Ti₂CT_x nanosheets gradually crimped, fractured (Fig. 1c), and finally converted into TiO₂ nanoparticles (Fig. 1d). Compared to some preparation technologies using harmful organic solvents, this water-based synthetic approach was nontoxic and green. Meanwhile, GO was converted into reduced graphene oxides (rGO) and an M-TiO₂@rGO gel was formed by a self-assembly process (Fig. 1e). As shown in the digital images (Fig. 1g), the obtained M-TiO₂@rGO gel sample supported a 100 g weight, exhibiting good mechanical character. The gel also exhibited a certain toughness that could be cut into self-supporting electrodes with a thickness of ~0.5 mm. Furthermore, the electrode retained good mechanical properties after drying (Fig. S1). A schematic diagram of the internal structure of the electrode is shown in Fig. 1f, in which a perpendicular porous structure is favorable for electrolyte soaking and enhancing the contact area between electrode and electrolyte, leading to a capable electrochemical performance.

To understand the stability of Ti₂CT_x and the formation mechanism of M-TiO₂ in water, the product and the supernatant after an ultrasonic process were collected and examined. The pH of the supernatant was about 3–4, which suggested that much H⁺ was generated and OH⁻ was consumed (Fig. S2). Thus, the formation of M-TiO₂ was mainly caused by the reactions between Ti₂CT_x and OH⁻ produced by the water decomposition, which was accelerated by the applied energy (ultrasonic and thermal energy in this case). Such a reaction might explain the instability of Ti₂CT_x in water and the unsatisfied electrocatalytic performance of Ti₂CT_x in the hydrogen evolution reaction

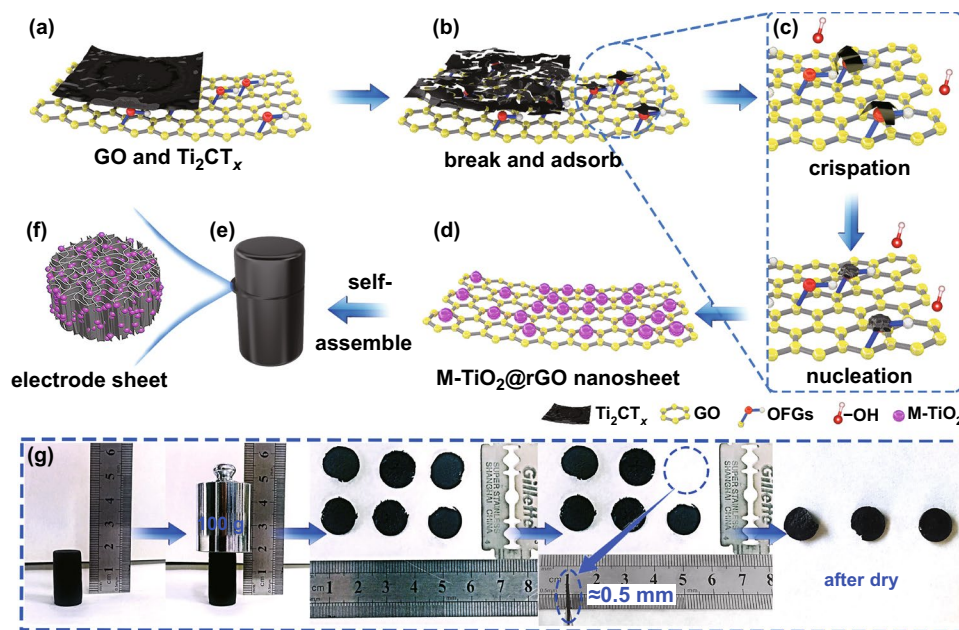


Fig. 1 The schematic and digital pictures of the M-TiO₂@rGO. **a** GO and Ti₂CT_x nanosheet; **b** Ti₂CT_x breaks and adsorbs on OFGs, and then **c** through crispation, finally, **d** reacts with OFGs and OH⁻ to form MXene-derived TiO₂; **e** M-TiO₂@rGO nanosheets through self-assemble process come into being composite gel; **f** internal structure of self-supporting electrode sheet; and **g** physical character of the M-TiO₂@rGO gel and self-supporting electrodes

[36]. Meanwhile, the supernatant was slightly yellow, compared with distilled water (Fig. S2b), which might be caused by suspended carbon nanomaterials derived from Ti₂CT_x. Also, transmission electron microscopy (TEM) images of the Ti₂CT_x products after different ultrasonic times showed pure Ti₂CT_x with intact lamellar morphology (Fig. S3a). After 5 h of sonication, some pores were observed in Ti₂CT_x nanosheets (Fig. S3b). With another 3 h of sonication, a large proportion of Ti₂CT_x nanosheets cracked into nanoparticles, but a small portion remained in a lamellar state (Fig. S3c). Finally, Ti₂CT_x nanosheets were completely converted into nanoparticles after 10 h of sonication (Fig. S3d) with 0.35 nm lattice spacing (Fig. S4), which was assigned to the (101) crystalline plane of anatase-TiO₂, suggesting the formation of TiO₂ nanoparticles [37]. In addition, the carbon layer could not be observed in the high rate TEM (HRTEM), further suggesting the carbon nanolayer exfoliation. Such a formation process was further confirmed by X-ray diffractometric (XRD) patterns of samples at different reaction times. First, Ti₂CT_x displayed a (002) characteristic peak in place of the highest peak of the Ti₂AlC at 39.5°, after the removal of Al layers in the Ti₂AlC (Fig. S5) [38]. During

the ultrasonic process, Ti₂CT_x was converted into an intermediate product with an amorphous phase (after 5 h sonication) and finally formed the anatase M-TiO₂ (Fig. S6). The microscopic appearance of M-TiO₂ was observed by scanning electron microscopy (SEM), showing serious agglomeration (Fig. S7). Thus, 2D GO nanosheets were necessary because they not only provided much oxygen source and active sites for the formation of M-TiO₂ but uniformly dispersed M-TiO₂ to improve the electrochemical utilization rate.

The morphology of the M-TiO₂@rGO foam was observed by SEM and TEM, which presented a poriferous honeycomb-like structure composed of numerous M-TiO₂/rGO nanosheets (Fig. 2a). On rGO nanosheets, M-TiO₂ nanoparticles cracked from MXene was again confirmed and evenly distributed on the surface (Figs. 2b and S8). This structure of the horizontal arrangement would be beneficial for preserving the sheet structure of graphene and accelerating electronic and sodium ion transportation by the rGO base. TEM images of M-TiO₂@rGO further confirmed the uniform distribution of TiO₂ on the rGO nanosheets (Fig. 2c, d), with an average particle size of ~15 nm, which could shorten sodium ion transportation in the materials. The

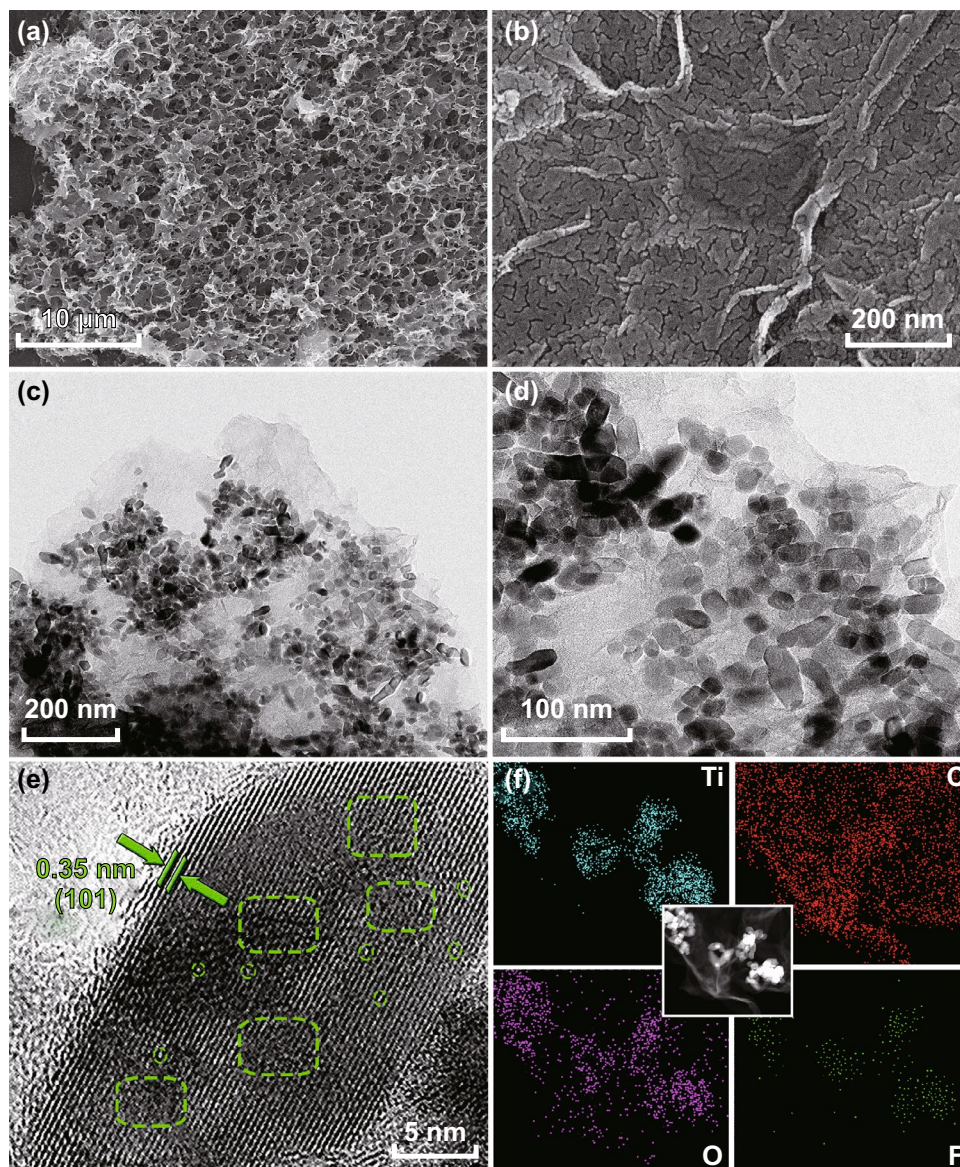


Fig. 2 Microscopic morphology of M-TiO₂@rGO foam. **a, b** SEM images; **c, d** TEM images; **e** HR-TEM image; and **f** dark field TEM and EDS mapping of C, O, Ti, and F

small difference in the particle size was attributed to the uneven dissociation of Ti₂CT_x nanosheets. In addition, rGO had few-layers structure according to the wrinkle thickness and observable lattice fringes (Fig. S9). An HRTEM image displayed clear crystal planes with a *d*-spacing of 0.35 nm, corresponding to the (101) lattice plane of anatase-TiO₂ [37]. Significantly, M-TiO₂ presented a large number of lattice defects with distortion and vacancy (Figs. 2e and S10), which might fundamentally improve the ion/electronic conductivity of TiO₂ [31]. Recent studies have also

proved that defective engineering was highly beneficial to increasing reactive sites and improving ions diffusion, thereby enhancing electrochemical performance [19, 39]. To further investigate M-TiO₂@rGO, EDS was performed, which showed the distribution of C, O, and Ti atoms in the composite. Interestingly, F inherited from Ti₂CT_x surface groups was also observed in composite (Fig. 2f) and pure M-TiO₂ (Fig. S11), which might be a cause for the defects in the TiO₂. Moreover, pure anatase M-TiO₂ exhibited a tan color rather than the white of commercial TiO₂ (Fig. S12),

and interestingly, peacock-blue rutile-TiO₂ could be also synthesized by adjusting the pH and controlling the reaction conditions (Fig. S13), which was caused by the oxygen vacancy and heteroatom doping [19, 31, 40, 41].

The structures of M-TiO₂ and M-TiO₂@rGO foam were investigated by XRD (Fig. 3a). Peaks located at 25.3°, 37.8°, 48.0°, 53.9°, 55.0°, and 62.7° corresponded to (101), (004), (200), (105), (211), and (204) crystal face of anatase TiO₂ (PDF#21-1272), respectively [7, 42]. The hump of M-TiO₂@rGO at ~26° was enhanced due to the existence of rGO [15]. Using the Scherrer formula based on the XRD results [9], the average crystalline sizes of M-TiO₂ and M-TiO₂@rGO were calculated to be ~18 and 12 nm, respectively (Table S1). This implied that the addition of rGO limited the TiO₂ growth. To further confirm the structure of M-TiO₂@rGO, a Raman spectrum was performed (Fig. 3b), in which peaks located at 149, 199, 397, 513, and 639 cm⁻¹ were assigned to the E_g, E_g, B_{1g}, A_{1g}, and E_g modes of anatase-TiO₂, respectively [15], and the peaks at 1354 and 1600 cm⁻¹ were denoted as the disorder and

graphitic peaks (D and G bands, respectively) [37]. After the hydrothermal reaction, the I_D/I_G of the M-TiO₂@rGO composite (1.01) was higher than that of GO (0.92), which was assigned to the intercalation of M-TiO₂ and nonstacking nature of M-TiO₂@rGO compared to pure graphene [15, 43]. Meanwhile, the content of M-TiO₂ in the composite was found to be ~67 wt%, according to thermogravimetric analysis (TG, Fig. S14). To understand the defect state and F doping, the X-ray photoelectron spectroscopy (XPS) test was performed (Figs. 3c and S15). From Fig. S15b, c, the attachment relation of M-TiO₂ and rGO was confirmed by the presence of the Ti–O–C bond [44, 45]. This also indicated that the OFGs on GO was involved in the formation of M-TiO₂. In addition, the F-Ti bond was observed at 684.6 eV due to F doping (Fig. S15a) [46]. Significantly, the Ti 2p_{3/2} and Ti 2p_{1/2} core level peaks could be divided into Ti³⁺ and Ti⁴⁺, due to lattice defects [37, 45]. In the oxygen signal, 530.5 eV could be assigned to lattice oxygen, and the obvious signal at 532.5 eV was caused by oxygen vacancies (Fig. S15c) [21]. Moreover, electron paramagnetic resonance

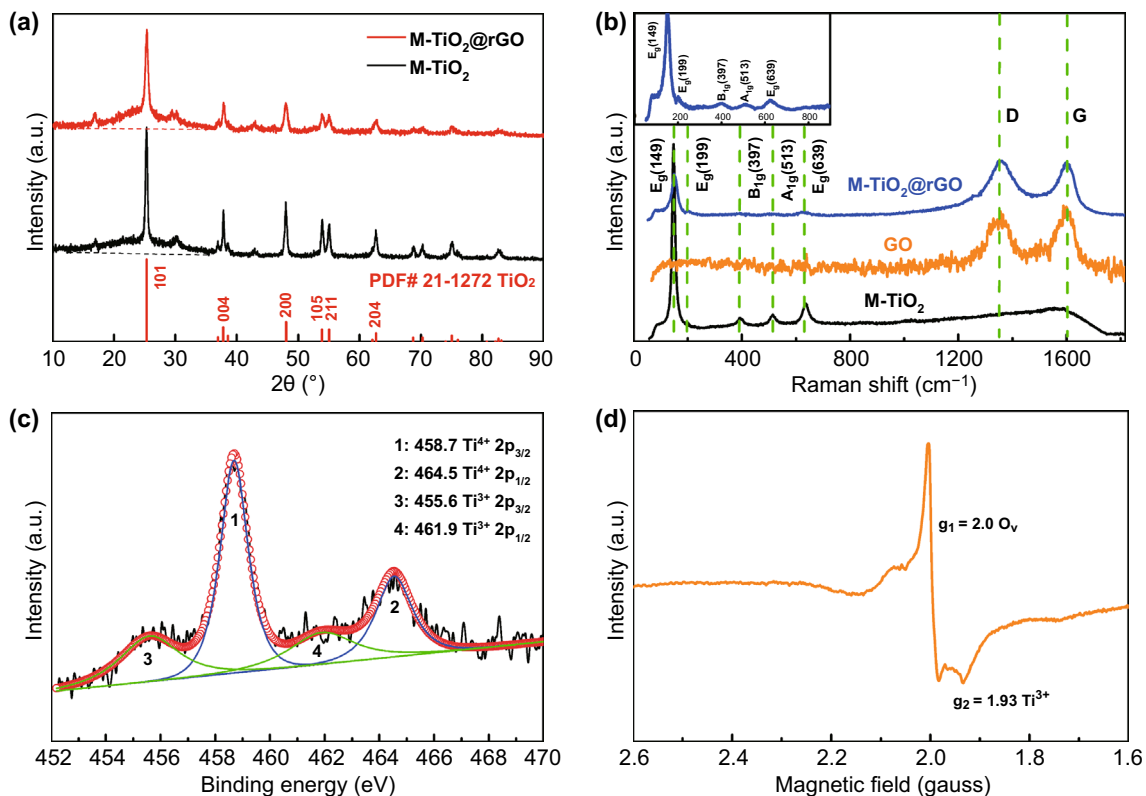


Fig. 3 Structure characterization of M-TiO₂@rGO composite. **a** XRD of M-TiO₂ and M-TiO₂@rGO; **b** Raman of M-TiO₂, GO, and M-TiO₂@rGO; **c** XPS curve of Ti 2p; and **d** EPR curve of M-TiO₂@rGO

(EPR) detection, a method to directly reveal oxygen vacancies, further confirmed the defect state (Fig. 3d). The strong signal at $g=2.0$ confirmed the existence of abundant oxygen vacancies and $g=1.93$ represented Ti^{3+} due to charge compensation during defective M-TiO_2 formation [21, 37, 40]. These above results strongly revealed that the massive lattice defects were mainly caused by the presence of a large number of oxygen vacancies and F doping, which could be attributed to the advantages of using the MXene parent phase. Furthermore, $\text{M-TiO}_2@\text{rGO}$ presented a specific surface area of $174 \text{ m}^2 \text{ g}^{-1}$ with an abundance of micropores and mesopores, shown by the nitrogen adsorption–desorption isotherms (Fig. S16). Such a hierarchical porous structure was very beneficial for electrolyte soaking, resulting in large contact areas between the electrode and electrolyte.

3.2 Electrochemical Performance and Kinetics Analysis of $\text{M-TiO}_2@\text{rGO}$ Electrode

$\text{M-TiO}_2@\text{rGO}$ foam could be applied directly as a self-supporting electrode. In sodium ion half cells, a remarkable rate performance was observed with average discharge specific capacities of 308, 223, 193, 171, 150, and 142 mAh g^{-1} at current densities of 50, 100, 200, 500, 1000, and 2000 mA g^{-1} , respectively (Fig. 4a). The average voltage of the $\text{M-TiO}_2@\text{rGO}$ electrode was $\sim 0.7 \text{ V}$ (Fig. 4b), which effectively avoided dendrite generation. The sloping discharge profiles demonstrated a possible pseudocapacitive behavior [15]. In addition, a common irreversible capacity was observed in the first discharge and cyclic voltammetry (CV) curves (Fig. S17a, b), with a Coulombic efficiency of 28%. The irreversible capacity was related to some irreversible transformation between Ti^{3+} and Ti^{4+} , irreversible insertion of sodium into porous structure, irreversible decomposition of the electrolyte, and the formation of solid electrolyte interphase (SEI) [15, 47, 48]. The *ex-situ* XRD curves of $\text{M-TiO}_2@\text{rGO}$ after the first discharge, first charge, and 1000 cycles showed that the peaks of $\text{M-TiO}_2@\text{rGO}$ were preserved, which demonstrated that the original structure remained unchanged during the sodiation or desodiation process (Fig. 4c). Even after 1000 cycles, the main peaks remained, suggesting favorable structural stability after repeated sodium ion insertion and desorption. Interestingly and typically, the $\text{M-TiO}_2@\text{rGO}$ electrode presented an electrochemical activation process during the initial

cycles (Fig. 4d), in which the 2nd, 3rd, 5th, and 10th cycles represented after 2, 3, 5, and 10 cycles of galvanostatic charge–discharge testing (current density of 50 mA g^{-1}), respectively. With cycling, a couple of anode/cathode peaks gradually appeared and became stable. Even after 1000 cycles, the anode/cathode peaks still remained well, suggesting a highly reversible sodium ion storage process. Such phenomena might have been caused by the transition of sodium ion storage from the surface to the bulk phase. This also suggested that $\text{M-TiO}_2@\text{rGO}$ presented multiple sodium ion storage mechanisms.

The cycling performance of the self-supporting $\text{M-TiO}_2@\text{rGO}$ electrode presented capacity retention of 97.2% after 1000 cycles at 1.0 A g^{-1} (Fig. 4e). Moreover, it demonstrated a capacity of 123.3 mAh g^{-1} with a capacity retention of 90.7% after 5000 cycles at 5.0 A g^{-1} , corresponding to a decay of 0.018% per cycle, which was better than previous reports regarding sodium-based self-supporting anodes [8, 49–51]. From SEM images after 1000 cycles, M-TiO_2 nanoparticles did not show shedding or agglomeration but only smooth edges, demonstrating good stability (Fig. S18). Electrochemical impedance spectroscopy (EIS) presented a reduced electrochemical reaction resistance and more pseudocapacitance diffusion behaviors after 1000 cycles (Fig. S19), which were attributed to activation process during the cycling. In addition, it was noticed that the capacity contribution from rGO was negligible (Fig. S20) and pure M-TiO_2 exhibited a poor electrochemical performance due to severe agglomeration phenomenon (Fig. S21). Thus, the observed superior electrochemical performance of $\text{M-TiO}_2@\text{rGO}$ was attributed to the synergistic effects of rGO and defect-rich M-TiO_2 . The former provided a stable framework and enhanced electronic conductivity, while the later enhanced electrolyte soaking and provided many reaction active sites.

To reveal the Na ion storage mechanism, a series of kinetic analyses for $\text{M-TiO}_2@\text{rGO}$ electrodes were performed as shown in Fig. 5. Figure 5a shows the CV curves from 0.2 to 100 mV s^{-1} . The electrochemical kinetics of Na ion storage was analyzed through the relation of the peak current (i) and scan rate (v):

$$i = av^b \quad (3)$$

In Eq. (3), the b -value is between 0.5 and 1, in which the two ends represent the diffusion-controlled process and the capacitance-controlled process, respectively [15]. The b -value evaluated as the logarithm of Eq. (3) showed that

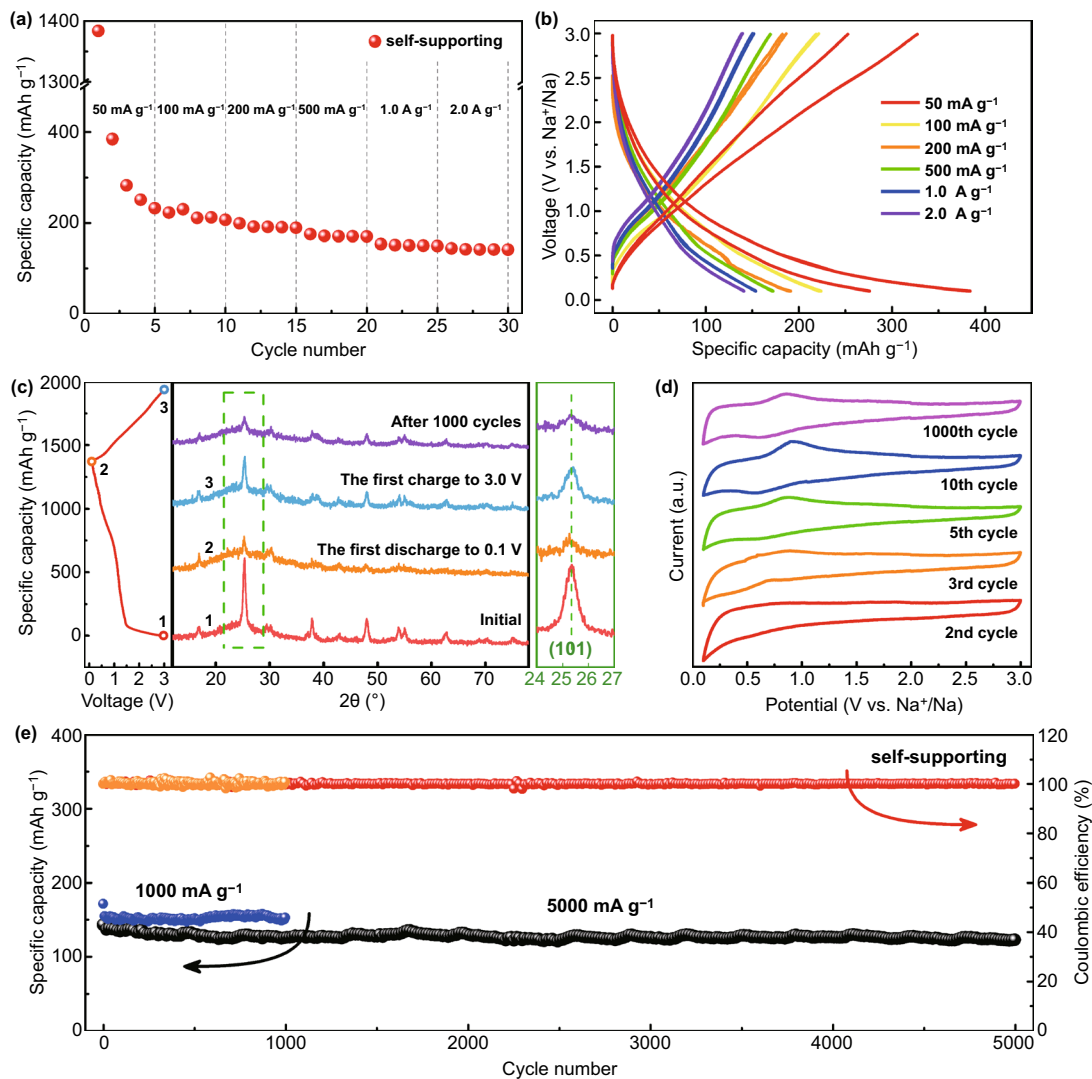


Fig. 4 Electrochemical characterization of the self-supporting M-TiO₂@rGO electrode in half cells. **a** Rate performance; **b** charge–discharge curves between 0.1 and 3.0 V from 50 mA g⁻¹ to 2.0 A g⁻¹; **c** XRD curves at different charging and discharging stages; **d** CV curves after galvanostatic charging–discharging tests with different cycles; and **e** 1000 and 5000 cycles cycling performance at 1.0 and 5.0 A g⁻¹

the *b* of anode peaks was 0.94 and the *b* of the cathode was 0.93, at sweep rates range from 0.2 to 5.0 mV s⁻¹ (Fig. 5b). This indicated that a capacitive process dominated the Na ion storage, leading to fast kinetics during charging and discharging. When the sweep rate was > 5.0 mV s⁻¹, the *b* of the anode decreased to 0.65, implying that the diffusion process was the restrictive step [52]. The charge (*Q*) versus *v*^{-1/2} plot more intuitively illustrated the results (Fig. 5b, inset). When the sweep rate was < 5.0 mV s⁻¹, the total charge did not change considerably with increased scan rates, which was because the capacitor behavior was less affected by the change of sweep speed. However, when the sweep rate was

> 5 mV s⁻¹, the charge decreased linearly with *v*^{-1/2}, indicating that it was controlled by the diffusion process [22]. The above results suggested that the M-TiO₂@rGO electrode contained two different types of sodium ion storage mechanisms and their presence directly affected the electrochemical performance. The ratios of the capacitance and diffusion contributions were determined using Eq. (4) [9]:

$$I(V) = k_1 v + k_2 v^{1/2} \tag{4}$$

in which, *I*-value is the currents at a particular voltage and different scan rates, *v* is the scan rates, *k*₁*v* and *k*₂*v*^{1/2} represent surface and diffusion control, respectively [15]. The

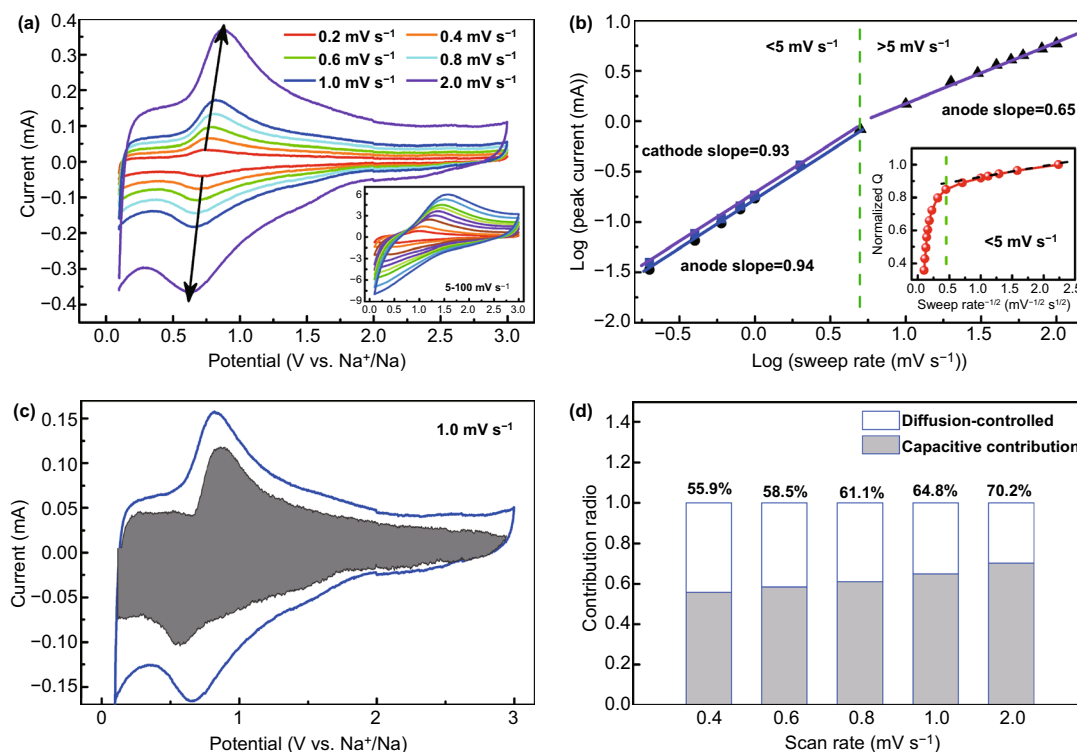


Fig. 5 Kinetics analysis of sodium ion storage behavior in the M-TiO₂@rGO electrode. **a** CV curves at different scan rates, inset: from 5 to 100 mV s⁻¹; **b** *b*-value analysis through the relation of the peak current (*i*) and the scan rate (*v*); inset: normalized charge versus scan rate^{-1/2}; **c** capacitive contribution area (gray) at the 1.0 mV s⁻¹; and **d** capacitive contribution ratios at 0.4–2 mV s⁻¹

specific algorithms can be seen in the Supporting Information and the results showed in Figs. S22 and 5c, d. The CV area (gray) of capacitive contribution at 1.0 mV s⁻¹ was displayed in Fig. 5c. The ratios of capacitive capacity showed a gradually increasing phenomenon as scan rates and a large capacitance contribution of 70.2% was obtained at 2.0 mV s⁻¹ (Fig. 5d). Based on the above results, the observed capable rate and stable cycling performance could be ascribed to the improved electron conductivity and ions diffusion as well as a large pseudocapacitance contribution, arising from the in nanoscale and defect engineering.

3.3 Sodium Ion Battery and Capacitor Based on M-TiO₂@rGO Universal Anode

The M-TiO₂@rGO foam electrode presented a lower working voltage, remarkable rate ability, and excellent cycling stability, demonstrating potential application as a universal anode for both SIBs and SICs. Thus, M-TiO₂@rGO//

Na₃V₂(PO₄)₃ SIBs and M-TiO₂@rGO//biomass-derived active carbon SICs were designed and assembled.

A SIB with Na₃V₂(PO₄)₃ (NVP) as the cathode and activated M-TiO₂@rGO as the anode was assembled. Before that, the electrochemical performance of NVP was investigated in a Na ion half-cell at the voltage window of 2.0–4.3 V. The charge/discharge profiles at different current densities were shown in Fig. S23a, with a charging platform of 3.4 V and a discharging platform of 3.3 V at 50 mA g⁻¹. A stable cycling performance with capacity retention of 85% was obtained after 200 cycles at 500 mA g⁻¹ (Fig. S23b). To better match the qualities of anode and cathode to ensure electrochemical performance, M-TiO₂@rGO was coated onto copper foil to flexibly regulate the mass loads of active materials. The rate performance of the coating-M-TiO₂@rGO electrode showed higher specific capacities than self-supporting M-TiO₂@rGO electrodes and other published reports at the same conditions (Fig. S24a). Furthermore, this half-cell exhibited an amazing cycling performance. At an

ultra-high current density of 10 A g^{-1} , a capacity of 127.2 mAh g^{-1} and capacity retention of 84.6% were still obtained after 10,000 cycles (Fig. S24b).

The electrochemical performance of SIBs was optimized by setting the electrode mass ratio at 1:3 (anode: cathode). The galvanostatic charge–discharge test was operated at 1.0–3.4 V. The $\text{M-TiO}_2\text{/rGO//NVP}$ full cell presented average capacities of 247.4, 200.3, 178.3, 148.3, and 135.8 mAh g^{-1} at current densities of 50, 200, 500, 1000, and 2000 mA g^{-1} , respectively, demonstrating a good rate performance (Fig. 6a). With current density increased, the shapes of the charge/discharge profiles retained well (Fig. 6b). In addition, the cycle stability was tested at the current density of 500 mA g^{-1} (Fig. 6c). The $\text{TiO}_2\text{/rGO//NVP}$ full cell exhibited a discharge capacity of 177.1 mAh g^{-1} in the first cycle and capacity retention of 74% (130.7 mAh g^{-1}) after 200 cycles. Meanwhile, the Coulomb efficiency tended to 100%, indicating a perfect kinetics match between the cathode and anode. It should be noted that the decreased capacity of the full cell was mainly caused by the cathode, based on the results of half cells. Thus, if $\text{M-TiO}_2\text{/rGO}$ was matched

with other more stable cathodes, the electrochemical performance would be further improved.

To achieve Na-based energy storage devices with higher power density, a SIC was assembled with activated $\text{M-TiO}_2\text{/rGO}$ as the anode and a 3D hierarchical porous activated carbon (HPAC) derived from coir [35] as the cathode. The electrochemical performance of the HPAC in Na-ion half-cell was measured at 3.0–4.2 V, with outstanding rate and cycling performances (Fig. S25). A typical electric double layer capacitor (EDLC) behavior of HPAC was demonstrated in the rectangular CV curves and triangular chronopotential potential (CP) curves (Fig. S25a, c). To better match the quality between the positive and negative electrodes to ensure electrochemical performance, the coating- $\text{M-TiO}_2\text{/rGO}$ electrode was used as the anode. The schematic of the SIC is shown in Fig. 7a. In the charging stage, Na^+ intercalated into the $\text{M-TiO}_2\text{/rGO}$ anode from the electrolyte, while ClO_4^- anions adsorbed on the HPAC cathode to balance the charge in electrolyte [53]. During the discharge stage, a reverse reaction occurred. To obtain higher energy density and cycling stability, the working

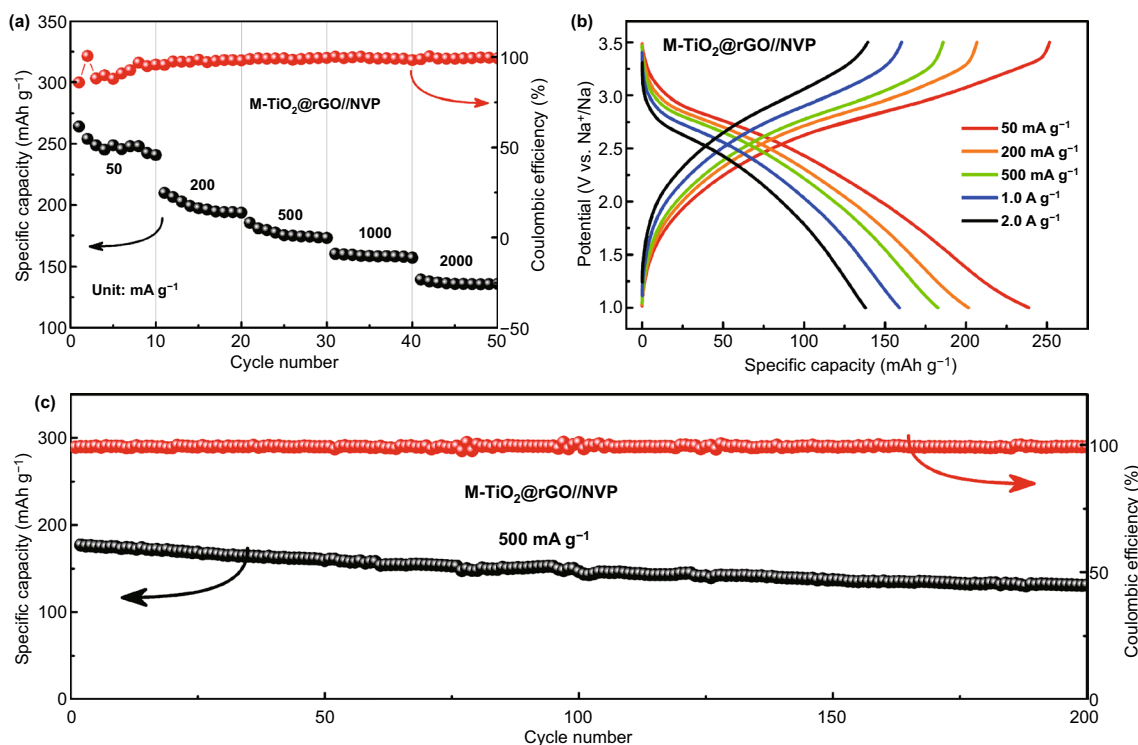


Fig. 6 Electrochemical performance of the sodium ion batteries (SIBs) with the NVP as cathodes and coated $\text{M-TiO}_2\text{/rGO}$ as anodes. **a** Rate performance; **b** charge–discharge curves at different current densities; and **c** cycling performance at 500 mA g^{-1}

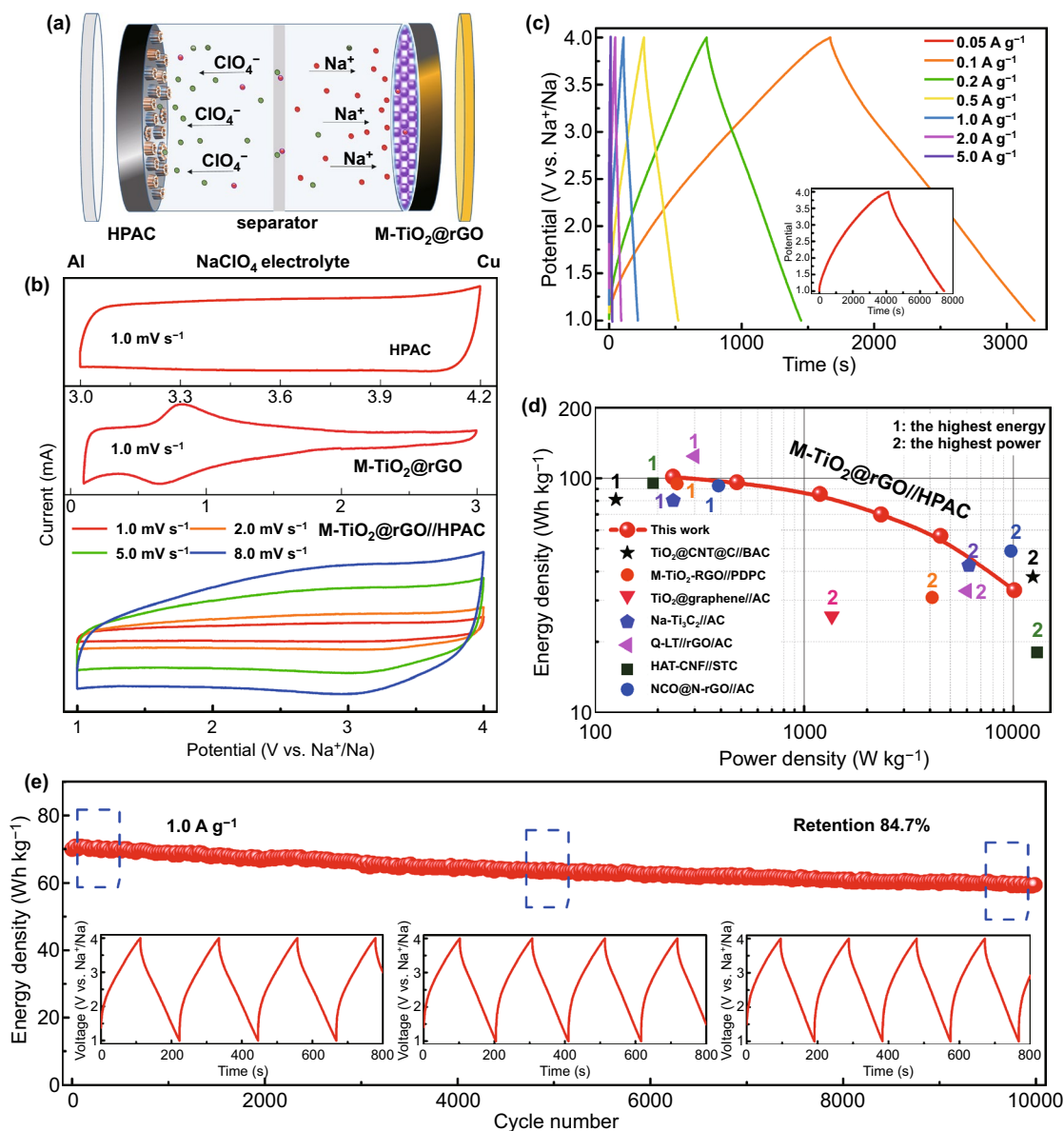


Fig. 7 Electrochemical performance of the sodium ion capacitors (SICs) with HPAC as cathodes and coated $M\text{-TiO}_2@r\text{GO}$ as anodes. **a** Schematic of the SICs; **b** CV curves of HPAC, $M\text{-TiO}_2@r\text{GO}$, and $M\text{-TiO}_2@r\text{GO}/\text{HPAC}$; **c** CP curves at different current densities; **d** Ragone plot of power density and energy density; and **e** cycling performance at 1.0 A g^{-1} , inset: CP curves at different states

voltage range of the SIC was selected to be 1.0–4.0 V [23]. The optimal mass ratio was investigated via rate and cycling performance tests (Fig. S26), which was set at 1:1.0, 1:1.5, 1:2.0, and 1:3.0 for anode/cathode. The device with a mass ratio of 1:1.5 displayed higher energy density and the best cycling performance, with capacity retention of 88.6% after 1000 cycles (2.0 A g^{-1}).

The optimized SICs with a mass ratio of 1:1.5 and an operating voltage window of 1.0–4.0 V were chosen to

further estimate the electrochemical performance (Fig. 7). The CV curves before and after assembly are shown in Fig. 7b, and the CV curves of SIC displayed an approximate rectangle with a slight peak attributed to certain pseudocapacitance reactions at high voltage, which was beneficial for achieving high energy density. Based on galvanostatic charge–discharge measurements, the typical near-linear CP curves at 1.0–4.0 V indicated a near ideal capacitive property, which implied rapid ion storage kinetics (Fig. 7c)

[56]. The energy and power densities were calculated based on the total masses of the anode and cathode. A superhigh energy density of 124.3 Wh kg^{-1} was obtained in the first cycle. After 5 cycles activation process at 0.05 A g^{-1} , a high energy density of 101.2 Wh kg^{-1} was achieved at a power density of 236.0 W kg^{-1} (0.1 A g^{-1}) and an ultrahigh power density of $10,103.7 \text{ W kg}^{-1}$ was obtained at an energy density of 33.2 Wh kg^{-1} (5.0 A g^{-1}). Such a remarkable electrochemical performance was at the top level compared to previous SICs reports (Fig. 7d), such as $\text{TiO}_2@\text{CNT}@\text{C}//\text{BAC}$ [9], $\text{M-TiO}_2\text{-RGO}//\text{PDPC}$ [23], $\text{TiO}_2@\text{graphene}//\text{AC}$ [7], $\text{HAT-CNF}//\text{STC}$ [54], $\text{Na-Ti}_3\text{C}_2//\text{AC}$ [55], $\text{NCO}@\text{N-rGO}//\text{AC}$ [47], and $\text{Q-LT}//\text{rGO}//\text{AC}$ [53]. Moreover, these SICs presented a long-term stable cycling performance with an energy retention ratio of 84.7% after 10,000 cycles at 1.0 A g^{-1} (Fig. 7e). In addition, no deformation occurred in the charge/discharge profiles, which further illustrated an excellent reversibility and perfect dynamics match between the anode and cathode. The above results suggest favorable designs are found here for the anode and cathode of Na-ion capacitors, which will provide a feasible strategy for the practical application of sodium ion energy storage devices.

4 Conclusions

In summary, Ti_2CT_x -derived defective TiO_2 nanoparticles were synthesized via a facile and environmentally friendly approach, Ti_2CT_x MXene aqueous phase splitting, in which the TiO_2 formation mechanism of Ti_2CT_x binding to OH^- produced by water decomposition was first revealed. Employing MXene parent phase achieved rich oxygen vacancies and F-doped metal oxides nanoparticles in situ, which fundamentally improved electrons/ions conductivity. Furthermore, an $\text{M-TiO}_2@\text{rGO}$ foam was synthesized and exhibited a hierarchical porous structure, which benefitted electrolyte permeation and enhanced ion transport. Employed as a free-standing anode for Na ion half cells, this material showed excellent rate performance and ultra-long cycling stability, with a retention ratio of 90.7% even after 5000 cycles at 5.0 A g^{-1} . Electrochemical analysis demonstrated pseudocapacitance-dominated hybrid sodium storage mechanism. At 2.0 mV s^{-1} , capacitive contribution is $\sim 70\%$, which was caused by the defects and nano-size particles. Finally, the distinctive $\text{M-TiO}_2@\text{rGO}$ electrode displayed a suitable electrochemical performance as a universal anode

for both $\text{M-TiO}_2@\text{rGO}//\text{NVP}$ SIBs and $\text{M-TiO}_2@\text{rGO}//\text{HPAC}$ SICs. The SICs showed a high energy density of 101.2 Wh kg^{-1} at a power density of 236.0 W kg^{-1} and an ultrahigh power density of $10,103.7 \text{ W kg}^{-1}$ at a mezzo energy density of 33.2 Wh kg^{-1} , along with outstanding cyclic stability with energy retention ratio of 84.7% after 10,000 cycles at 1.0 A g^{-1} . This study will facilitate the rapid development of anodes for high-performance sodium-based energy storage devices and inspire more applications for MXene.

Acknowledgements This work was supported by the National Natural Science Foundation of China (51702063, 51672056), Natural Science Foundation of Heilongjiang (LC2018004), China Postdoctoral Science Foundation (2018M630340, 2019T120254) and the Fundamental Research Funds for the Central University.

Open Access This article is licensed under a Creative Commons Attribution 4.0 International License, which permits use, sharing, adaptation, distribution and reproduction in any medium or format, as long as you give appropriate credit to the original author(s) and the source, provide a link to the Creative Commons licence, and indicate if changes were made. The images or other third party material in this article are included in the article's Creative Commons licence, unless indicated otherwise in a credit line to the material. If material is not included in the article's Creative Commons licence and your intended use is not permitted by statutory regulation or exceeds the permitted use, you will need to obtain permission directly from the copyright holder. To view a copy of this licence, visit <http://creativecommons.org/licenses/by/4.0/>.

Electronic supplementary material The online version of this article (<https://doi.org/10.1007/s40820-020-00471-9>) contains supplementary material, which is available to authorized users.

References

1. B. Dunn, H. Kamath, J.-M. Tarascon, Electrical energy storage for the grid: a battery of choices. *Science* **334**(6058), 928–935 (2011). <https://doi.org/10.1126/science.1212741>
2. M. Park, J. Ryu, W. Wang, J. Cho, Material design and engineering of next-generation flow-battery technologies. *Nat. Rev. Mater.* **2**(1), 16080 (2017). <https://doi.org/10.1038/natrevmats.2016.80>
3. C. Vaalma, D. Buchholz, M. Weil, S. Passerini, A cost and resource analysis of sodium-ion batteries. *Nat. Rev. Mater.* **3**(4), 18013 (2018). <https://doi.org/10.1038/natrevmats.2018.13>
4. S. Li, Z. Zhao, C. Li, Z. Liu, D. Li, $\text{SnS}_2@\text{C}$ hollow nanospheres with robust structural stability as high-performance

- anodes for sodium ion batteries. *Nano-Micro Lett.* **11**(1), 14 (2019). <https://doi.org/10.1007/s40820-019-0243-7>
5. Y. Jiang, X. Zhou, D. Li, X. Cheng, F. Liu, Y. Yu, Highly reversible Na storage in $\text{Na}_3\text{V}_2(\text{PO}_4)_3$ by optimizing nanostructure and rational surface engineering. *Adv. Energy Mater.* **8**(16), 1800068 (2018). <https://doi.org/10.1002/aenm.201800068>
 6. J. Zhao, X. Yang, Y. Yao, Y. Gao, Y. Sui et al., Moving to aqueous binder: a valid approach to achieving high-rate capability and long-term durability for sodium-ion battery. *Adv. Sci.* **5**(4), 1700768 (2018). <https://doi.org/10.1002/advs.201700768>
 7. Z. Le, F. Liu, P. Nie, X. Li, X. Liu et al., Pseudocapacitive sodium storage in mesoporous single-crystal-like TiO_2 -graphene nanocomposite enables high-performance sodium-ion capacitors. *ACS Nano* **11**(3), 2952–2960 (2017). <https://doi.org/10.1021/acsnano.6b08332>
 8. Z. Xia, H. Sun, X. He, Z. Sun, C. Lu, In situ construction of CoSe_2 @vertical-oriented graphene arrays as self-supporting electrodes for sodium-ion capacitors and electrocatalytic oxygen evolution. *Nano Energy* **60**, 385–393 (2019). <https://doi.org/10.1016/j.nanoen.2019.03.052>
 9. Y.E. Zhu, L. Yang, J. Sheng, Y. Chen, H. Gu, J. Wei, Z. Zhou, Fast sodium storage in TiO_2 @CNT@C nanorods for high-performance Na-ion capacitors. *Adv. Energy Mater.* **7**(22), 1701222 (2017). <https://doi.org/10.1002/aenm.201701222>
 10. Y. Sun, S. Guo, H. Zhou, Exploration of advanced electrode materials for rechargeable sodium-ion batteries. *Adv. Energy Mater.* **9**, 1800212 (2018). <https://doi.org/10.1002/aenm.201800212>
 11. F. Wu, C. Zhao, S. Chen, Y. Lu, Y. Hou, Y.S. Hu, J. Maier, Y. Yan, Multi-electron reaction materials for sodium-based batteries. *Mater. Today* **21**(9), 960–973 (2018). <https://doi.org/10.1016/j.mattod.2018.03.004>
 12. C. Peng, H. Chen, G. Zhong, W. Tang, Y. Xiang et al., Capacity fading induced by phase conversion hysteresis within alloying phosphorus anode. *Nano Energy* **58**, 560–567 (2019). <https://doi.org/10.1016/j.nanoen.2019.01.035>
 13. P. Bai, Y. He, P. Xiong, X. Zhao, K. Xu, Y. Xu, Long cycle life and high rate sodium-ion chemistry for hard carbon anodes. *Energy Storage Mater.* **13**, 274–282 (2018). <https://doi.org/10.1016/j.ensm.2018.02.002>
 14. S. Guo, Q. Li, P. Liu, M. Chen, H. Zhou, Environmentally stable interface of layered oxide cathodes for sodium-ion batteries. *Nat. Commun.* **8**(1), 135 (2017). <https://doi.org/10.1038/s41467-017-00157-8>
 15. Y. Fang, R. Hu, B. Liu, Y. Zhang, K. Zhu et al., Mxene-derived TiO_2 /reduced graphene oxide composite with an enhanced capacitive capacity for Li-ion and K-ion batteries. *J. Mater. Chem. A* **7**(10), 5363–5372 (2019). <https://doi.org/10.1039/C8TA12069B>
 16. L. Sang, L. Lei, C. Burda, Electrochemical fabrication of rGO-embedded Ag– TiO_2 nanoring/nanotube arrays for plasmonic solar water splitting. *Nano-Micro Lett.* **11**(1), 97 (2019). <https://doi.org/10.1007/s40820-019-0329-2>
 17. Q. Gan, H. He, Y. Zhu, Z. Wang, N. Qin, S. Gu, Z. Li, W. Luo, Z. Lu, Defect-assisted selective surface phosphorus doping to enhance rate capability of titanium dioxide for sodium ion batteries. *ACS Nano* **13**(8), 9247–9258 (2019). <https://doi.org/10.1021/acsnano.9b03766>
 18. C. Li, T. Wang, Z.J. Zhao, W. Yang, J.F. Li et al., Promoted fixation of molecular nitrogen with surface oxygen vacancies on plasmon-enhanced TiO_2 photoelectrodes. *Angew. Chem. Int. Ed.* **57**(19), 5278–5282 (2018). <https://doi.org/10.1002/anie.201713229>
 19. Y. Zhang, Z. Ding, C.W. Foster, C.E. Banks, X. Qiu, X. Ji, Oxygen vacancies evoked blue TiO_2 (B) nanobelts with efficiency enhancement in sodium storage behaviors. *Adv. Funct. Mater.* **27**(27), 1700856 (2017). <https://doi.org/10.1002/adfm.201700856>
 20. L. Huang, X. Zhou, R. Xue, P. Xu, S. Wang et al., Low-temperature growing anatase TiO_2 /SnO₂ multi-dimensional heterojunctions at MXene conductive network for high-efficient perovskite solar cells. *Nano-Micro Lett.* **12**(1), 44 (2020). <https://doi.org/10.1007/s40820-020-0379-5>
 21. W. Zhang, L. Cai, S. Cao, L. Qiao, Y. Zeng et al., Electrode materials: interfacial lattice-strain-driven generation of oxygen vacancies in an aerobic-annealed TiO_2 (B) electrode. *Adv. Mater.* **31**(52), 1970367 (2019). <https://doi.org/10.1002/adma.201970367>
 22. B. Li, B. Xi, Z. Feng, Y. Lin, J. Liu, J. Feng, Y. Qian, S. Xiong, Hierarchical porous nanosheets constructed by graphene-coated, interconnected TiO_2 nanoparticles for ultrafast sodium storage. *Adv. Mater.* **30**(10), 1705788 (2018). <https://doi.org/10.1002/adma.201705788>
 23. R. Wang, S. Wang, Y. Zhang, D. Jin, X. Tao, L. Zhang, Graphene-coupled Ti_3C_2 MXenes-derived TiO_2 mesostructure: promising sodium-ion capacitor anode with fast ion storage and long-term cycling. *J. Mater. Chem. A* **6**(3), 1017–1027 (2018). <https://doi.org/10.1039/C7TA09153B>
 24. X. Zhang, J. Li, J. Li, L. Han, T. Lu, X. Zhang, G. Zhu, L. Pan, 3D TiO_2 @nitrogen-doped carbon/ Fe_7S_8 composite derived from polypyrrole-encapsulated alkalized MXene as anode material for high-performance lithium-ion batteries. *Chem. Eng. J.* **385**, 123394 (2020). <https://doi.org/10.1016/j.cej.2019.123394>
 25. P. Nakhanej, X. Yu, S.K. Park, S. Kim, J.-Y. Hong et al., Revealing molecular-level surface redox sites of controllably oxidized black phosphorus nanosheets. *Nat. Mater.* **18**(2), 156–162 (2019). <https://doi.org/10.1038/s41563-018-0230-2>
 26. X. Yu, S. Yun, J.S. Yeon, P. Bhattacharya, L. Wang, S.W. Lee, X. Hu, H.S. Park, Emergent pseudocapacitance of 2D nanomaterials. *Adv. Energy Mater.* **8**(13), 1702930 (2018). <https://doi.org/10.1002/aenm.201702930>
 27. Y. Fang, Y. Zhang, K. Zhu, R. Lian, Y. Gao et al., Lithiophilic three-dimensional porous $\text{Ti}_3\text{C}_2\text{T}_x$ -rGO membrane as a stable scaffold for safe alkali metal (Li or Na) anodes. *ACS Nano* **13**(12), 14319–14328 (2019). <https://doi.org/10.1021/acsnano.9b07729>
 28. H. He, Q. Gan, H. Wang, G.-L. Xu, X. Zhang et al., Structure-dependent performance of TiO_2 /C as anode material for

- Na-ion batteries. *Nano Energy* **44**, 217–227 (2018). <https://doi.org/10.1016/j.nanoen.2017.11.077>
29. Y. Xing, S. Wang, B. Fang, G. Song, D.P. Wilkinson, S. Zhang, N-doped hollow urchin-like anatase TiO₂@C composite as a novel anode for Li-ion batteries. *J. Power Sources* **385**, 10–17 (2018). <https://doi.org/10.1016/j.jpowsour.2018.02.077>
 30. Y. Zhu, L. Peng, Z. Fang, C. Yan, X. Zhang, G. Yu, Structural engineering of 2D nanomaterials for energy storage and catalysis. *Adv. Mater.* **30**(15), 1706347 (2018). <https://doi.org/10.1002/adma.201706347>
 31. A. Naldoni, M. Allieta, S. Santangelo, M. Marelli, F. Fabbri et al., Effect of nature and location of defects on bandgap narrowing in black TiO₂ nanoparticles. *J. Am. Chem. Soc.* **134**(18), 7600–7603 (2012). <https://doi.org/10.1021/ja3012676>
 32. Q. Wu, J.P. Zheng, M. Hendrickson, E.J. Plichta, Dry process for fabricating low cost and high performance electrode for energy storage devices. *MRS Adv.* **4**(15), 857–863 (2019). <https://doi.org/10.1557/adv.2019.29>
 33. S. Wang, Q. Wang, W. Zeng, M. Wang, L. Ruan, Y. Ma, A new free-standing aqueous zinc-ion capacitor based on MnO₂-CNTs cathode and MXene anode. *Nano-Micro Lett.* **11**(1), 70 (2019). <https://doi.org/10.1007/s40820-019-0301-1>
 34. Y. Zhu, S. Murali, W. Cai, X. Li, J.W. Suk, J.R. Potts, R.S. Ruoff, Graphene and graphene oxide: synthesis, properties, and applications. *Adv. Mater.* **22**(35), 3906–3924 (2010). <https://doi.org/10.1002/adma.201001068>
 35. L. Yin, Y. Chen, X. Zhao, B. Hou, B. Cao, 3-Dimensional hierarchical porous activated carbon derived from coconut fibers with high-rate performance for symmetric supercapacitors. *Mater. Design* **111**, 44–50 (2016). <https://doi.org/10.1016/j.matdes.2016.08.070>
 36. Z.W. Seh, K.D. Fredrickson, B. Anasori, J. Kibsgaard, A.L. Strickler et al., Two-dimensional molybdenum carbide (MXene) as an efficient electrocatalyst for hydrogen evolution. *ACS Energy Lett.* **1**(3), 589–594 (2016). <https://doi.org/10.1021/acscenergylett.6b00247>
 37. H. He, Q. Zhang, H. Wang, H. Zhang, J. Li, Z. Peng, Y. Tang, M. Shao, Defect-rich TiO₂- δ nanocrystals confined in a mooncake-shaped porous carbon matrix as an advanced Na ion battery anode. *J. Power Sources* **354**, 179–188 (2017). <https://doi.org/10.1016/j.jpowsour.2017.04.035>
 38. H. Xu, X. Yin, X. Li, M. Li, S. Liang, L. Zhang, L. Cheng, Lightweight Ti₂CT_x MXene/poly (vinyl alcohol) composite foams for electromagnetic wave shielding with absorption dominated feature. *ACS Appl. Mater. Interfaces* **11**, 10198–10207 (2019). <https://doi.org/10.1021/acsami.8b21671>
 39. Y. Zhao, Y. Zhao, R. Shi, B. Wang, G.I. Waterhouse, L.Z. Wu, C.H. Tung, T. Zhang, Tuning oxygen vacancies in ultrathin TiO₂ nanosheets to boost photocatalytic nitrogen fixation up to 700 nm. *Adv. Mater.* **31**(16), 1806482 (2019). <https://doi.org/10.1002/adma.201806482>
 40. Y. Yang, K. Ye, D. Cao, P. Gao, M. Qiu, L. Liu, P. Yang, Efficient charge separation from F-selective etching and doping of anatase-TiO₂ {001} for enhanced photocatalytic hydrogen production. *ACS Appl. Mater. Interfaces* **10**(23), 19633–19638 (2018). <https://doi.org/10.1021/acsami.8b02804>
 41. L. Hüttenhofer, F. Eckmann, A. Lauri, J. Cambiasso, E. Pensa et al., Anapole excitations in oxygen vacancy-rich TiO_{2-x} nanoresonators: tuning the absorption for photocatalysis in the visible. *ACS Nano* **14**, 2456–2464 (2020). <https://doi.org/10.1021/acsnano.9b09987>
 42. H. Ren, R. Yu, J. Qi, L. Zhang, Q. Jin, D. Wang, Hollow multishelled heterostructured anatase/TiO₂ (B) with superior rate capability and cycling performance. *Adv. Mater.* **31**(10), 1805754 (2019). <https://doi.org/10.1002/adma.201805754>
 43. N.A. Kumar, R.R. Gaddam, S.R. Varanasi, D. Yang, S.K. Bhatia, X. Zhao, Sodium ion storage in reduced graphene oxide. *Electrochim. Acta* **214**, 319–325 (2016). <https://doi.org/10.1016/j.electacta.2016.08.058>
 44. B. Ahmed, D.H. Anjum, M.N. Hedhili, Y. Gogotsi, H.N. Alshareef, H₂O₂ assisted room temperature oxidation of Ti₂C MXene for Li-ion battery anodes. *Nanoscale* **8**(14), 7580–7587 (2016). <https://doi.org/10.1039/C6NR00002A>
 45. C. Chen, Y. Wen, X. Hu, X. Ji, M. Yan et al., Na⁺ intercalation pseudocapacitance in graphene-coupled titanium oxide enabling ultra-fast sodium storage and long-term cycling. *Nat. Commun.* **6**, 6929 (2015). <https://doi.org/10.1038/ncomms7929>
 46. J.A. Khan, C. Han, N.S. Shah, H.M. Khan, M.N. Nadagouda et al., Ultraviolet–visible light–sensitive high surface area phosphorous–fluorine–co-doped TiO₂ nanoparticles for the degradation of atrazine in water. *Environ. Eng. Sci.* **31**(7), 435–446 (2014). <https://doi.org/10.1089/ees.2013.0486>
 47. D. Yang, Q. Zhao, L. Huang, B. Xu, N.A. Kumar, X.S. Zhao, Encapsulation of NiCo₂O₄ in nitrogen-doped reduced graphene oxide for sodium ion capacitors. *J. Mater. Chem. A* **6**(29), 14146–14154 (2018). <https://doi.org/10.1039/C8TA03411G>
 48. D. Yan, C. Yu, D. Li, X. Zhang, J. Li, T. Lu, L. Pan, Improved sodium-ion storage performance of TiO₂ nanotubes by Ni²⁺ doping. *J. Mater. Chem. A* **4**(28), 11077–11085 (2016). <https://doi.org/10.1039/C6TA04906K>
 49. L. Wang, G. Yang, J. Wang, S. Wang, C. Wang, S. Peng, W. Yan, S. Ramakrishna, In situ fabrication of branched TiO₂/C nanofibers as binder-free and free-standing anodes for high-performance sodium-ion batteries. *Small* **15**, 1901584 (2019). <https://doi.org/10.1002/smll.201901584>
 50. G. Xu, L. Yang, Z. Li, X. Wei, P.K. Chu, Protein-assisted assembly of mesoporous nanocrystals and carbon nanotubes for self-supporting high-performance sodium electrodes. *J. Mater. Chem. A* **5**(6), 2749–2758 (2017). <https://doi.org/10.1039/C6TA09673E>
 51. G. Xu, Y. Tian, X. Wei, L. Yang, P.K. Chu, Free-standing electrodes composed of carbon-coated Li₄Ti₅O₁₂ nanosheets and reduced graphene oxide for advanced sodium ion batteries. *J. Power Sources* **337**, 180–188 (2017). <https://doi.org/10.1016/j.jpowsour.2016.10.088>
 52. V. Augustyn, J. Come, M.A. Lowe, J.W. Kim, P.-L. Taberna, S.H. Tolbert, H.D. Abruña, P. Simon, B. Dunn, High-rate



- electrochemical energy storage through Li^+ intercalation pseudocapacitance. *Nat. Mater.* **12**(6), 518 (2013). <https://doi.org/10.1038/nmat3601>
53. L.F. Que, F.D. Yu, X.L. Sui, L. Zhao, J.G. Zhou, D.-M. Gu, Z.-B. Wang, Thermal-induced interlayer defect engineering toward super high-performance sodium ion capacitors. *Nano Energy* **59**, 17–25 (2019). <https://doi.org/10.1016/j.nanoen.2019.02.030>
54. R. Yan, E. Josef, H. Huang, K. Leus, M. Niederberger et al., Understanding the charge storage mechanism to achieve high capacity and fast ion storage in sodium-ion capacitor anodes by using electrospun nitrogen-doped carbon fibers. *Adv. Funct. Mater.* **29**, 1902858 (2019). <https://doi.org/10.1002/adfm.201902858>
55. J. Luo, F. Cong, C. Jin, H. Yuan, O. Sheng et al., Tunable pseudocapacitance storage of MXene by cation pillaring for high-performance sodium ion capacitors. *J. Mater. Chem. A* **6**(17), 7794–7806 (2018). <https://doi.org/10.1039/C8TA02068J>
56. N.A. Kumar, J.-B. Baek, Doped graphene supercapacitors. *Nanotechnology* **26**(49), 492001 (2015). <https://doi.org/10.1088/0957-4484/26/49/492001>